Front. Med. 2025, 19(1): 101−120
https://doi.org/10.1007/s11684-024-1093-3

RESEARCH ARTICLE

Mitochondrial-associated programmed-cell-death patterns for predicting the prognosis of non-small-cell lung cancer

Xueyan Shi, Sichong Han, Guizhen Wang, Guangbiao Zhou (✉)

State Key Laboratory of Molecular Oncology & Department of Medical Oncology, National Cancer Center/National Clinical Research Center for Cancer/Cancer Hospital, Chinese Academy of Medical Sciences and Peking Union Medical College, Beijing 100021, China

Abstract **Mitochondria are the convergence point of multiple pathways that trigger programmed cell death (PCD). Mitochondrial-associated PCD (mtPCD) is involved in the pathogenesis of several diseases. However, the role of mtPCD in the prognostic prediction of cancers including non-small-cell lung cancer (NSCLC) remains to be investigated. Here, 12 mtPCD patterns were analyzed in transcriptomics, genomics, and clinical data collected from 4 datasets containing 977 patients. A risk-score assessment system containing 18 genes was established. We found that NSCLC patients with a high-risk score had a poorer prognosis. A nomogram was constructed by incorporating the risk score with clinical features. The risk score was further associated with clinicopathological information, tumor-mutation frequency, and immunotherapy responses. NSCLC patients with a high risk score had more Treg cells infiltration. However, these patients had higher tumor-mutation burden scores and may be more sensitive to immunotherapy. Moreover, receptor-interacting serine/threonine protein kinase 2 (RIPK2) was selected from mtPCD gene model for validation. We found that RIPK2 exhibited oncogenic function, and its expression level was inversely associated with the overall survival of NSCLC. Taken together, our results indicated the accuracy and practicability of the mtPCD gene model and RIPK2 in predicting the prognosis of NSCLC.**

Keywords mitochondrial associated programmed cell death; NSCLC; prognosis; gene signature

Introduction

Lung cancer is the most commonly occurring cancer worldwide and the leading cause of cancer deaths, with 2.5 million new cases and 1.8 million deaths each year [1]. Lung cancer comprises non-small-cell lung cancer (NSCLC) and small-cell lung cancer (SCLC), whereas NSCLC accounts for 85% of all lung cancer cases. It can be further divided into lung adenocarcinoma (LUAD, 40%), lung squamous cell carcinoma (30%), and large-cell carcinoma [2]. Over the past two decades, targeted therapies and immunotherapies have been used to treat NSCLC and significantly improve the clinical outcome of the patients [3-8]. However, the therapeutic efficacy of NSCLC remains unsatisfactory due to primary or acquired drug resistance and the heterogeneity and complexity of tumor tissues [9–13]. Moreover, current tumor-staging systems cannot accurately predict the prognosis of patients with different molecular features [14]. Therefore, biomarkers for predicting responses to individualized treatment are urgently needed.

Cell death can be classified as accidental or programmed cell death (PCD), with the latter being a complex regulatory process that involves multiple mechanisms *in vivo* [15]. To date, at least 12 modes of PCD have been reported, including necroptosis, autophagy, pyroptosis, ferroptosis, apoptosis, NETotic cell death, alkaliptosis, entotic cell death, cuproptosis, oxeiptosis, parthanatos, and lysosome-dependent cell death [16–18]. Apoptosis is the most extensively studied PCD modality that leads to immunogenicity or induces no immunogenic response in different contexts [19]. Necroptosis is initiated by the activation of cell-surface death receptors and RNA- and DNA-sensing molecules in cells. Necroptosis is characterized by the permeabilization of the plasma membrane, cell swelling, and loss of cellular and organelle integrity [20, 21]. Pyroptosis, a recently discovered type of PCD, is characterized by caspase-1 dependence and the release of numerous

Received April 30, 2024; accepted May 20, 2024
Correspondence: Guangbiao Zhou, gbzhou@cicams.ac.cn

pro-inflammatory factors [22, 23]. Ferroptosis is a mode of cell death in which iron-dependent accumulation of lipid peroxidation reaches lethal levels [24, 25]. Cuprotosis is characterized by the excessive accumulation of copper ions, leading to abnormal aggregation of lipoacylated proteins, interference with mitochondrial respiration, and ultimately cell death [26]. Autophagy is the major intracellular-degradation pathway through which cytoplasmic materials are delivered and degraded in lysosomes [27]. NETotic cell death is an inflammatory cell death mode of neutrophils, that captures and kills pathogens by releasing cell-trapping nets into the extracellular matrix [28]. Parthanatos is a novel form of PCD caused by DNA damage and activation of poly(ADP-ribose) polymerase PARP-1 [29]. Lysosome-dependent cell death occurs through the cathepsin-mediated cleavage and activation of key regulators of apoptosis [30]. Alkaliptosis is a form of cell death that is driven by intracellular alkalization [31]. Entotic cell death is a mode of cell death that involves the death of epithelial cells and the formation of glandular cavities [32]. Oxeiptosis is a caspase-independent apoptosis-like cell death process induced by reactive oxygen species [33]. Multiple forms of PCD work together to regulate cell fate. Mitochondria are organelles that play pivotal roles in various cellular processes, including metabolism, energy production, and calcium homeostasis. They serve as convergence points of multiple pathways that trigger PCD [34]. Mitochondrial-associated PCD (mtPCD) is involved in the pathogenesis of several diseases [35, 36], but its roles in cancer pathogenesis and prognosis prediction in many cancers including NSCLC remain to be investigated.

The present study aimed to evaluate the mtPCD status in NSCLC and the association between mtPCD and the efficacy of therapeutic interventions among patients. Using 4 datasets containing 977 NSCLC patients and 1210 mtPCD genes, we found the ability of mtPCD genes to predict the heterogeneity in patients with NSCLC and evaluate their clinical prognosis. It may also help in selecting appropriate treatment options for patients with NSCLC.

Materials and methods

Candidate genes and data collection

The mitochondrion-related gene set was derived from two databases, namely, MitoProteome (1705 genes) and MitoCarta3.0 (1135 genes). After merging the two databases and removing duplicate genes, the total number of genes was 1903. The gene set related to PCD was derived from literature [18], and the total number of genes was 1253 after duplication removal.

The correlation between mitochondrion-related gene sets and PCD gene sets was analyzed using The Cancer Genome Atlas (TCGA)-NSCLC dataset, as well as the Gene Expression Omnibus GSE29013, GSE31210, and GSE37745 datasets. The mtPCD gene-selection criteria were $|R| > 0.3$ and $P < 0.05$. Univariate Cox regression analysis was performed to select mtPCD genes related to the prognosis of NSCLC. The screening criteria were $P < 0.05$ for overall survival (OS) based on survival curve analysis. The 1-, 3-, and 5-year areas under the receiver operating characteristic curve (ROC) curve (AUC) values analysis $\geqslant 0.55$.

Construction of prognostic model and external validation

All samples in the TCGA-NSCLC dataset were randomly divided into two groups (1:1, training and validation groups). The glmnet [37] package was used to conduct LASSO regression analysis according to the gene expression and clinical data related to prognosis obtained from the above screening in the training group. Finally, the marker genes were determined according to the LASSO regression results, and then the regression coefficients of each gene, the risk values of each sample, and the differences in the risk values for different pathological types were calculated. The GSE29013, GSE31210, and GSE37745 datasets were used to verify model stability. The predict.cv.glmnet function was used to calculate risk values for each sample.

Clinical characteristics and genomic and transcriptomic variations

Demographic characteristics of patients were obtained from the corresponding datasets. Initially, all samples were divided into high- and low-risk groups according to the above-mentioned median risk values. Differences in other clinical factors between the groups were compared using the chi-square test (categorical data) or the Wilcoxon test (continuous data). The maftools [38] package was used to explore the differences in the high- and low-risk groups at the genomic level and the gene-mutation frequency between the samples in the two groups. The limma package was used to explore differences at the transcription levels between the high- and low-risk groups and to identify differentially expressed genes (DEGs). The screening criteria were fold change (FC) > 2 and $P < 0.05$. Then, the cluterprofiler [39] package was used for functional-enrichment analysis. Based on these risk values, a prediction model was established to describe the impact of these factors influencing patients' 1-, 3-, and 5-year survival through multivariate regression models.

Tumor microenvironment and immune-cell infiltration

According to the expression of immune-cell marker genes in each sample, cibersort [40] was used to score the immune-cell infiltration. Statistical differences between the scores of different cells in the high- and low-risk groups were calculated using Wilcoxon test. TMEscore [41] package was used to estimate the specific tumor microenvironment of each sample. The Wilcoxon test was used to calculate the score difference between the high- and low-risk groups.

Cell culture and transfection

NSCLC cell lines A549 and H1299 (American Type Culture Collection, Manassas, VA, USA) were cultured in DMEM or RPMI 1640 medium supplemented with 10% fetal bovine serum (HyClone, Logan, UT, USA) at 37 °C in a 5% CO_2/95% air incubator. Transient transfection of siRNAs was conducted using a Lipofectamine 3000 kit (Invitrogen) according to the vendor's instructions. The sequences of si*RIPK2* were as follows: human receptor-interacting serine/threonine-protein kinase 2 (*RIPK2*) siRNA-1#: CUCUCACAGUCACGAAGUATT; and human *RIPK2* siRNA-2#: GCUGCAUUCUGUGAUCACATT

Cell viability and colony-formation assay

For cell-viability assay, cells were seeded onto 12-well plates, and the cell confluence area was monitored every 4 h over a 3-day period by using an IncuCyte Live-Cell Analysis System (Essen Bioscience). For colony formation, 500 cells were seeded onto six-well plates with 2 mL of medium in each well. The culture medium was replaced every three days. After 10 days of cultivation, the medium was removed and cells were fixed with 4% neutral paraformaldehyde for 30 min before staining with crystal violet for 20 min. Colonies more than 50 cells were counted under a microscope.

qPCR

Total RNA was extracted from cells using a SteadyPure Quick RNA Extraction kit (Accurate Biology). cDNA was synthesized using a HiScript III First-Strand cDNA Synthesis kit (Vazyme) [42]. qPCRs were performed using a SYBR Green Master Mix (Vazyme). The gene-specific primers were as follows (5′–3′): human RIPK2-S: GCCCTTGGTGTAAATTACCTGC; and human RIPK2-AS: GGACATCATGCGCCACTTT.

Immunoblotting analysis

Protein samples were prepared using RIPA lysis (Analysis Quiz, Beijing, China) added with a proteinase and phosphatase inhibitor cocktail (Analysis Quiz, Beijing, China). Equal amounts of proteins were subjected to polyacrylamide gel electrophoresis and transferred onto polyvinylidene fluoride membranes. The membranes were blocked in 5% milk and then incubated with the corresponding primary antibodies. Afterwards, an Horseradish Peroxidase (HRP)-linked secondary antibody (1:1000, Jackson) was used for chemiluminescence under the gel-imaging system.

Xenograft studies

The animal studies were approved by and conducted according to the Ethics Committee of Cancer Hospital, Chinese Academy of Medical Sciences. Six-week-old male NSG mice with severe combined immunodeficiency were purchased from Vital River Laboratory Animal Technology Co., Ltd. (Beijing, China), kept in a specific pathogen-free environment and used for the animal assays. After 7 days of acclimatization, 5×10^6 A549 cells were subcutaneously inoculated into the dorsal flank. Tumor volumes were measured every 3 days with following the formula: volume = 1/2 length × width [2]. Twenty-five days later, the mice were sacrificed.

Patient samples and IHC assay

This study was approved by the Research Ethics Committee of the Cancer Hospital, Chinese Academy of Medical Sciences and conducted in accordance with the *Declaration of Helsinki*. The diagnosis of lung cancer was confirmed by at least two pathologists. All lung-cancer samples were collected with informed consent. Human lung-cancer tissue arrays were purchased from Shanghai Outdo Biotech (Cat# HLugA180Su09). The samples were obtained from patients with written informed consent. IHC staining of human lung-cancer tissue arrays was performed according to the manufacturer's protocol (Zhongshan Golden Bridge, Beijing, China) [43]. IHC was quantified as immunoreactivity score (IRS; 0–12) = SP (0–1: 0%–25%; 2: 26%–50%; 3: 51%–75% and 4: > 75%) × SI (0: no signal; 1: weak; 2: moderate and 3: strong), where SP is the proportion of stained positive cells and SI is the staining intensity.

Statistical analysis

All statistical analyses were conducted using R software (v.4.1.0). Student's *t*-test was used to analyze the differences between two groups. Pearson correlation analysis was conducted to analyze the correlations between two continuous variables. Univariate and multivariate Cox regression analyses were performed for prognostic analysis. Survival curves were described using

Kaplan–Meier plots and compared using the log-rank test. $P < 0.05$ was considered statistically significant.

Results

mtPCD genes associated with the prognosis of NSCLC patients

A flowchart of the study is shown in Fig. 1A. We included patients of 4 datasets, including 500 from TCGA, 55 from GSE29013, 196 from GSE37745, and 226 from GSE31210. Meanwhile, 12 PCD patterns with 1253 genes were included in the analysis. To filter the mtPCD-related genes, correlation analysis was performed based on the mitochondrial- and PCD-related gene sets in the TCGA-NSCLC dataset. The genetic screening criterion was $|R| > 0.3$. Through correlation analysis of the genes, we found that most genes were associated with one another (Fig. 1B). A total of 1210 mtPCD genes were identified, and univariate Cox regression analysis was used to select candidate mtPCD genes related to the prognosis of NSCLC. The screening criteria were $P < 0.05$ of OS based on survival-curve analysis, as well as 1-, 3-, and 5-year AUC values of ROC analysis $\geqslant 0.55$. A total of 76 prognostic mtPCD genes were identified, including *ERO1A*, *VDAC1*, *BMP5*, *KRT8*, *PRKCD*, *YWHAG*, *PPP1R13B*, *AP3S1*, *YWHAZ*, and others (Table 1). Univariate Cox regression analysis presented results for only a subset of genes that were indeed related to the prognosis of NSCLC (Table 2).

Construction of a prognostic model for NSCLC patients

We explored whether a prognostic model of mtPCD genes can be constructed using a machine-learning method by performing LASSO regression analysis based on the expression of the 76 prognostic mtPCD genes and clinical data. The LASSO regression analysis was then cross-validated (Fig. 2A and 2B). Interestingly, a prognostic model containing 18 genes was constructed. These genes were *AP3S1*, *CCK*, *EIF2AK3*, *ERO1A*, *KRT8*, *PEBP1*, *PIK3CD*, *PPIA*, *PPP3CC*, *RAB39B*, *RIPK2*, *RUBCNL*, *SELENOK*, *SQLE*, *STK3*, *TRIM6*, *VDAC1*, and *VPS13D*. The risk score of each sample was calculated according to the fitted regression model and expression of each gene. All samples were divided into high- and low-risk groups according to the above-mentioned median risk value. We then compared OS among patients with NSCLC in high- and low-risk groups. Our results showed that patients with a high-risk score had a lower survival rate than those with a low-risk one (Fig. 2C). To verify the accuracy of the model, ROC curve analysis was performed on the internal training set, validation set, and all 500 NSCLC patients. Based on the ROC curve, the prognostic model constructed in this study can be used to predict the prognosis of patients with NSCLC. Moreover, the risk of death was high, and the survival time was relatively short in the high-risk group (Fig. 2D–2F). These results suggested that this model can work well independently in forecasting the prognosis of patients with NSCLC.

Correlation analysis between prognostic models and clinical features in NSCLC patients

To explore whether the risk scores were statistically significant among patients with different physiologic and pathological information, the Wilcoxon test was used to test the difference in risk scores between different groups. Results showed that the risk score was significantly correlated with age, sex, survival status (alive or dead), tumor stage T (T1–T4, T1/2, T3/4), N (N0–N3), M (M0–M1), and clinical stage (I–IV, I/II, III/IV) (Fig. 3A–3F). Patients with higher risk score had poorer prognosis (Fig. 3G). These results suggested that the risk value may be used to indicate different stages of progression in patients with NSCLC, and that a higher risk score implied an advanced tumor stage.

Establishment and assessment of a nomogram survival model

To verify the accuracy of the model in external datasets, the stability of the model was verified using the GSE29013, GSE31210, and GSE37745 datasets according to the expression of the genes used in the LASSO regression model construction (Fig. 4A–4C). Results showed that the model still had high accuracy in the external validation set, further proving the accuracy and robustness of the prognostic model. To further improve the prediction accuracy of the prognostic model and enhance the possibility of applying this model to clinical treatment, we combined the above risk scores and pathological stage information to construct a nomogram model (Fig. 4D). Based on the risk values, a prediction model was established using multivariate regression analysis to evaluate the impact of these factors influencing the 1-, 3-, and 5-year survival rates of patients. Calibration curves showed the accuracy of the model in predicting survival at different follow-up periods. Based on the nomogram score, a significant difference in OS existed between the high- and low-risk groups (Fig. 4E). Thus, our model had a high accuracy in predicting OS in patients with NSCLC.

Genomic variation landscape of mtPCD genes in NSCLC patients

All samples were divided into high- and low-risk groups

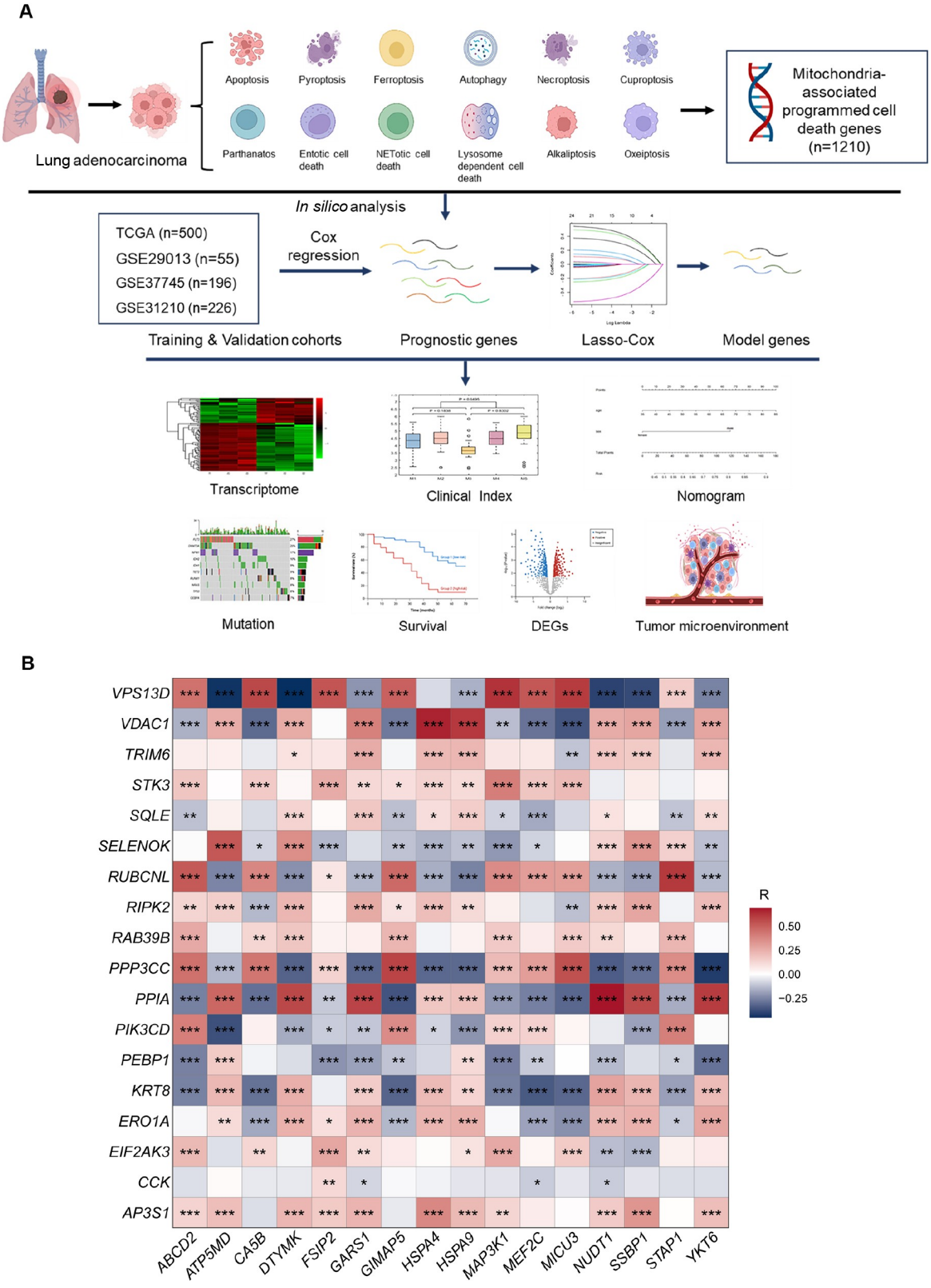

Fig. 1 Screening for mtPCD genes associated with prognosis in NSCLC patients. (A) Flowchart for comprehensive analysis of diverse cell-death patterns in NSCLC patients. (B) Heat map of association of different mtPCD genes associated with prognosis. *P* values, Pearson correlation analysis. **P* < 0.05, ***P* < 0.01, ****P* < 0.001.

Table 1 Top 76 mtPCD genes related to NSCLC prognosis

Gene	OS *P* value	OS HR	DFS *P* value	DFS HR
AATF	0.001463608	1.637884674	0.308581662	1.186694663
ADRB2	0.000604248	0.586783451	0.09361295	0.767756786
AP1S3	0.00013801	1.830730598	0.002734592	1.593666428
AP3S1	0.00035052	1.734925563	0.001713077	1.6322063
BLK	0.000450324	0.586853299	0.002182238	0.61832252
BMP5	1.69661E-05	0.531269978	0.001824955	0.632696875
BTK	1.25387E-05	0.509625905	0.025954598	0.718247452
CASP12	0.006229491	0.651146909	0.048065211	0.742370407
CCK	0.011364623	1.518838712	0.056254449	1.333347404
CD27	0.008530174	0.677279977	0.058667338	0.756363075
CD28	0.005346537	0.655666245	0.058064371	0.708197058
CD5	0.000600383	0.581476488	0.035232879	0.725172421
CD74	0.000346467	0.564492975	0.00489124	0.660616756
CD84	0.00148217	0.624228122	0.061604723	0.750903573
CISD2	7.43282E-05	2.009400428	0.002206274	1.660091375
CTSG	0.000515787	0.599836204	0.005028482	0.660809563
CTSL	0.000269075	1.753617433	0.000404122	1.699105363
CTSV	0.000360776	1.692902906	0.000459878	1.764772129
CX3CR1	0.002339807	0.588709383	0.002071365	0.615655051
CYCS	0.000141932	1.746765318	0.0003543	1.698684889
CYLD	0.000105289	0.493023575	0.03530879	0.716448187
EIF2AK3	0.00248305	0.566536084	0.207309978	0.813244057
ELAPOR1	4.69416E-05	0.545048077	0.000934998	0.602100327
ERO1A	1.72991E-08	2.308761917	1.23606E-05	1.940484527
FADD	2.89707E-06	1.980236422	0.001009753	1.624430941
FANCD2	0.001224555	1.639740584	0.034833108	1.365869545
FGF10	0.025853834	0.704876974	0.062574899	0.748375998
FYCO1	4.22601E-06	0.394491337	0.070303826	0.739952069
HERPUD1	1.18948E-05	0.525266669	0.000720863	0.608649778
HGF	0.00028576	0.482082888	0.017639155	0.650467375
HSP90AA1	0.002356783	1.568128873	0.007582392	1.4933947
IL10RA	0.002443754	0.597140434	0.06968509	0.757928567
IL33	0.000148129	0.492728938	0.108362227	0.775247982
KRT8	1.87106E-05	1.921793553	0.000279772	2.001893688
LCK	0.001033044	0.610992157	0.004407788	0.650872687
MIF	5.73635E-05	2.327339437	0.034781264	1.368812363
NEDD4	0.000222921	1.78520144	0.007459699	1.54465793
NLRP1	0.000619688	0.604227418	0.010107393	0.679309587
NUPR1	0.001491361	0.576194935	0.004747265	0.643667134
PDCD5	0.001350781	1.604207552	0.000312787	1.695257878
PEBP1	1.6554E-05	0.527650949	0.024595099	0.676331833
PERP	4.12061E-06	1.974890343	0.001553448	1.628653439
PGD	0.013766209	1.46899841	0.039115509	1.380257852
PIK3CD	6.75863E-05	0.549643338	0.008899778	0.679616211
PIK3CG	0.001048732	0.613834402	0.07046049	0.76133073

(*Continued*)

Gene	OS *P* value	OS HR	DFS *P* value	DFS HR
PIK3R1	0.000198072	0.572962756	0.003355229	0.648708142
PLA2G3	0.003314469	0.620287441	0.016750356	0.702103012
PLAUR	6.62913E-05	1.86356012	0.000575737	1.829533697
PPARD	0.002029731	1.607640345	0.02402129	1.399782249
PPIA	0.000124364	1.816781299	0.005836115	1.700710968
PPP1R13B	4.04041E-06	0.50780252	6.19671E-05	0.551762435
PPP3CC	0.000440629	0.57444117	0.252768019	0.838139045
PPT2	3.70653E-05	1.844849901	0.106183563	1.305604363
PRKCD	6.49679E-06	0.513349668	0.001541809	0.623699034
PSME3	7.90856E-05	1.813614351	0.016393077	1.43675576
PTGDS	5.25695E-05	0.450174895	0.02148952	0.661734867
PTPRC	0.00037879	0.59186307	0.028969459	0.722366829
RAB39B	0.000162437	0.538762159	0.001554661	0.607919379
RELA	0.001160967	1.634242426	0.040872423	1.359960781
RIPK2	7.70016E-05	2.16028144	0.001022995	1.828553237
RUBCNL	0.000386259	0.586121403	0.017276013	0.703229609
SAT2	0.002404408	0.622071555	0.011311364	0.670387286
SELENOK	6.77735E-06	0.509478831	0.019207581	0.699598887
SEPTIN4	0.007817973	0.670255718	0.068829314	0.746313656
SLC3A2	0.000597705	1.65705208	0.005777514	1.523037507
SQLE	9.04135E-05	1.77770124	0.186146891	1.227462497
STK3	0.004662917	1.648804417	0.09611093	1.321966677
TFEB	9.86438E-05	0.564766402	0.007177001	0.668665465
TNFRSF10C	0.000143015	0.570517944	0.012811751	0.692614953
TREM2	0.00688257	0.670983659	0.074978929	0.763089942
TRIM38	0.00250484	0.624506528	0.012401389	0.648360985
TRIM6	3.76238E-05	1.889016798	0.000110454	1.790602722
VDAC1	8.61136E-07	2.047677084	0.000369061	1.864258245
VPS13D	6.00218E-05	0.461774392	0.017240195	0.661682298
YWHAG	8.21208E-06	1.925603247	2.01286E-05	1.882515802
YWHAZ	2.98876E-05	1.851819866	0.001211367	1.721306015

P value, log-rank test.

Table 2 Top 9 genes related to NSCLC prognosis

Gene	OS *P* value	OS HR	DFS *P* value	DFS HR
ERO1A	1.81E-07	1.494367831	0.000801571	1.305294
VDAC1	1.72E-06	1.874563126	0.001354623	1.557407
BMP5	7.49E-06	0.858564858	0.002208029	0.893505
KRT8	1.21E-05	1.468094655	0.000599661	1.36051
PRKCD	3.96E-05	0.625692388	0.031784316	0.763687
YWHAG	4.57E-05	1.669970398	0.012667647	1.361472
PPP1R13B	6.57E-05	0.722842665	0.000345529	0.730916
AP3S1	9.49E-05	1.887382109	0.000655791	1.751243
YWHAZ	0.000155	1.616013334	0.000937533	1.550296

P value, log-rank test.

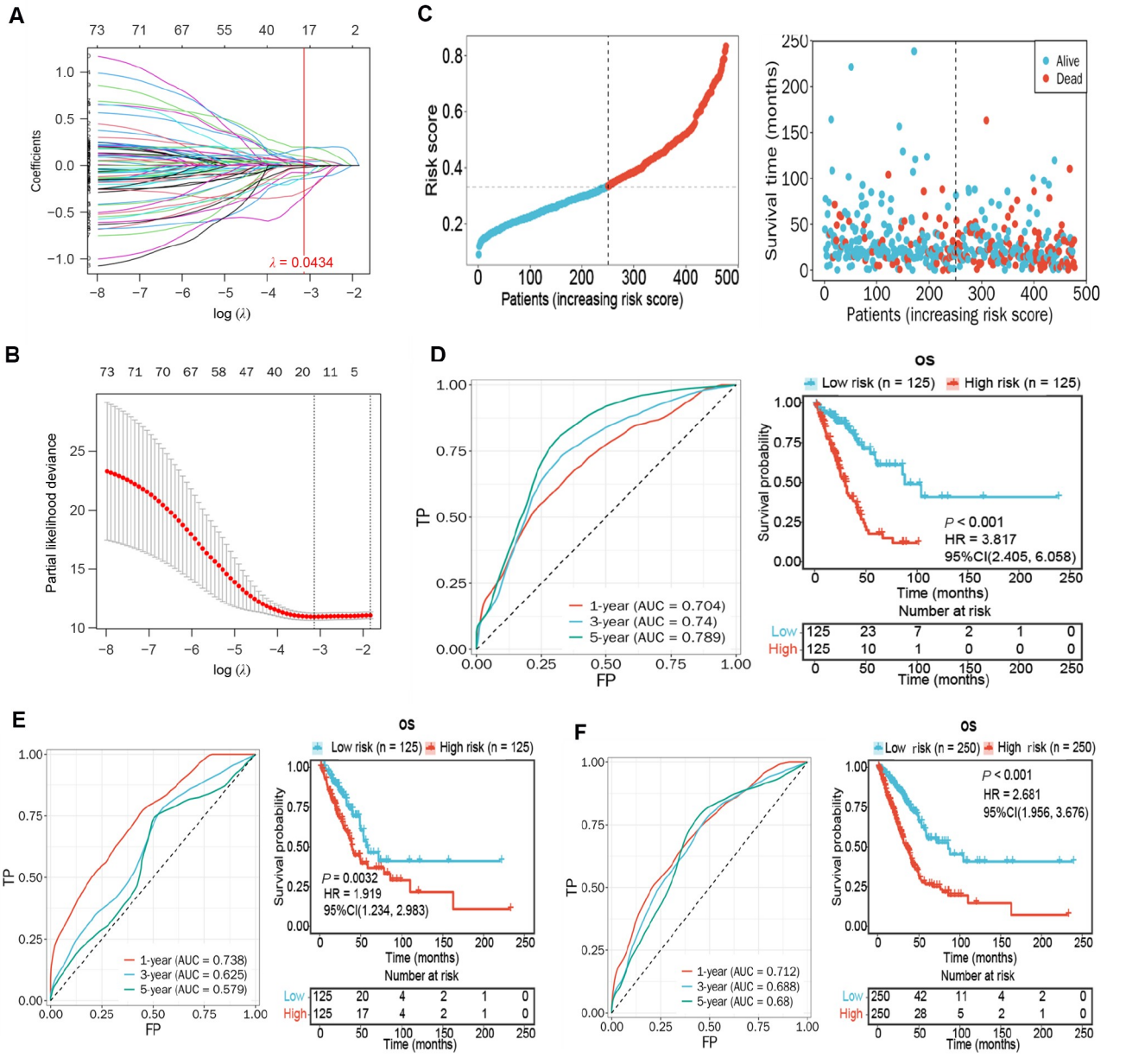

Fig. 2 Construction of a prognostic model for NSCLC patients. (A) Selection of 18 model genes by machine learning. (B) Cross-validation of the constructed signature. (C) Distribution of adjusted risk score according to the survival status and time in TCGA cohorts. (D) ROC of risk values and OS prognostic plots in the training group. (E) ROC of risk values and OS prognostic plots in the internal validation group. (F) ROC of risk values and OS prognostic plots in TCGA cohorts.

based on the median risk value of the prognostic model described above. We evaluated variants in mtPCD-related genes in patients with NSCLC from TCGA cohort. Our results showed that 440 (88.89%) of the 495 patients harbored mutations in their genome. The top 10 mutations of mtPCD-related genes are shown in Fig. 5A. Among them, *TP53* had the highest mutation frequency (48%), and the frequencies of the others ranged from 25% to 45%. The higher frequency of *TP53* mutation occurred in higher-risk patients with poor prognosis, and the mutations of *TP53* were often associated with a poor prognosis. This finding was consistent with the clinical result that high-risk patients had a poor prognosis. Considering the high-risk group as an example, we presented the mutation state of mtPCD genes in the following six ways: variant classification, variant type, single nucleotide variants class, variants per sample, variant classification summary, and the top 10 mutated genes (Fig. 5B). We summarized the top 10 gene-mutation frequencies and the differences in mutation frequency between the high- and low-risk groups and found that the mutation frequency of the high-risk group

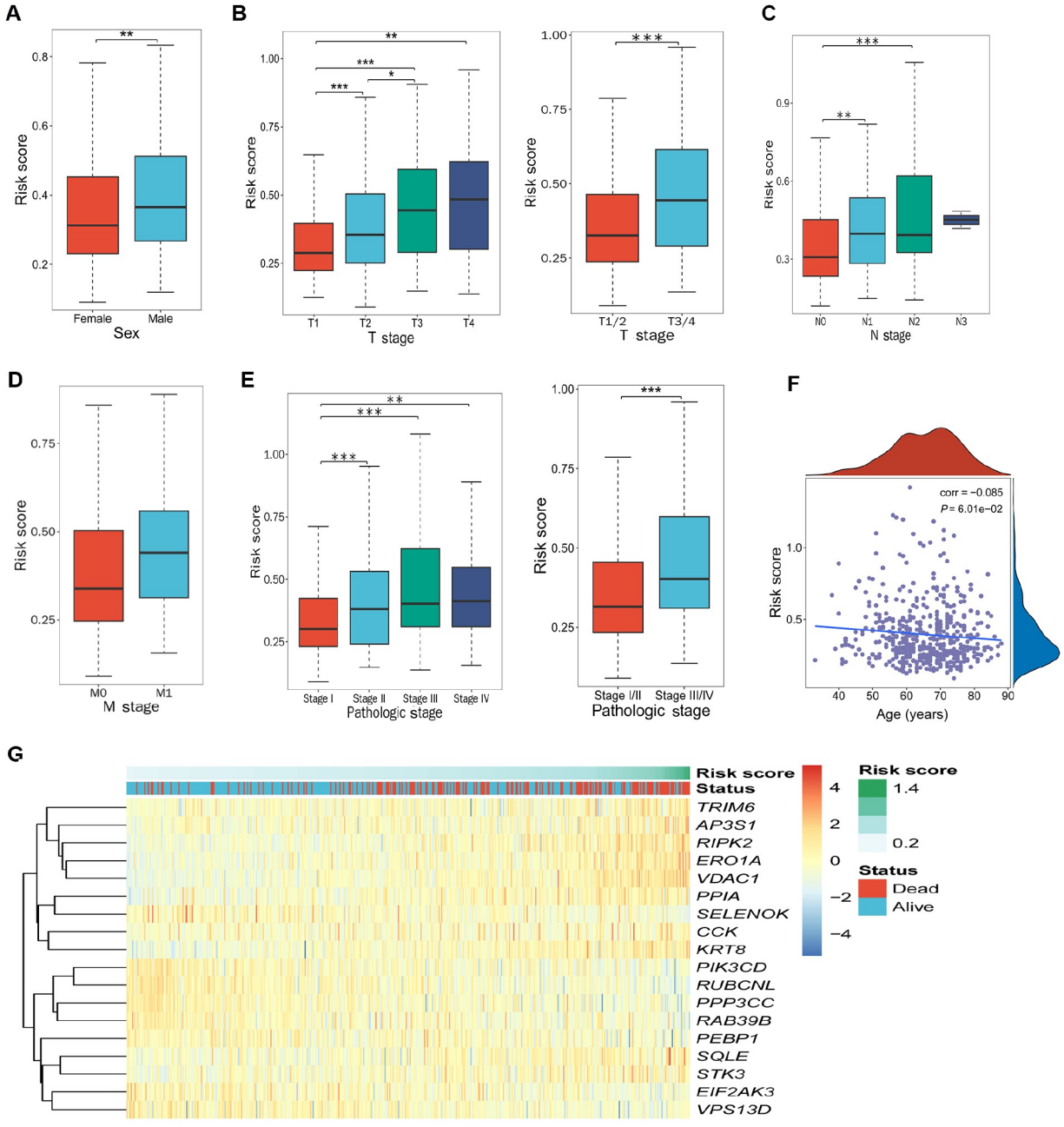

Fig. 3 Correlation analysis between prognostic models and clinical features in NSCLC patients. (A–F) Box and scatter plot of the relationship between risk value and age, sex, T, N, M, and clinical stage. *P* values, Student's *t* test. **P* < 0.05, ***P* < 0.01, ****P* < 0.001. (G) Heatmap of 18 model genes and survival status.

was significantly higher than that of the low-risk one (Fig. 5C and 5D). Simultaneously, we analyzed the correlation among the top 30 mutant genes and found that most of them were interrelated to varying degrees (Fig. 5E). We predicted and classified genes that can be targeted by drugs and found that mutated p53 can be targeted by multiple drug types (tumor suppressor, transcription factor complex, RNA directed DNA polymerase, histone modification, etc.; Fig. 5F), which may provide clues for future drug development.

Transcriptome variation landscape of mtPCD genes in NSCLC patients

In the TCGA-NSCLC cohort, a total of 829 differentially DEGs were obtained by differential enrichment analysis between high- and low- risk groups. Among them, 379 genes were upregulated and 450 were downregulated in the NSCLC group. The scaled RNA levels of DEGs are shown as volcano plots (Fig. 6A), and the top 20 differential genes are shown in the heat map (Fig. 6B).

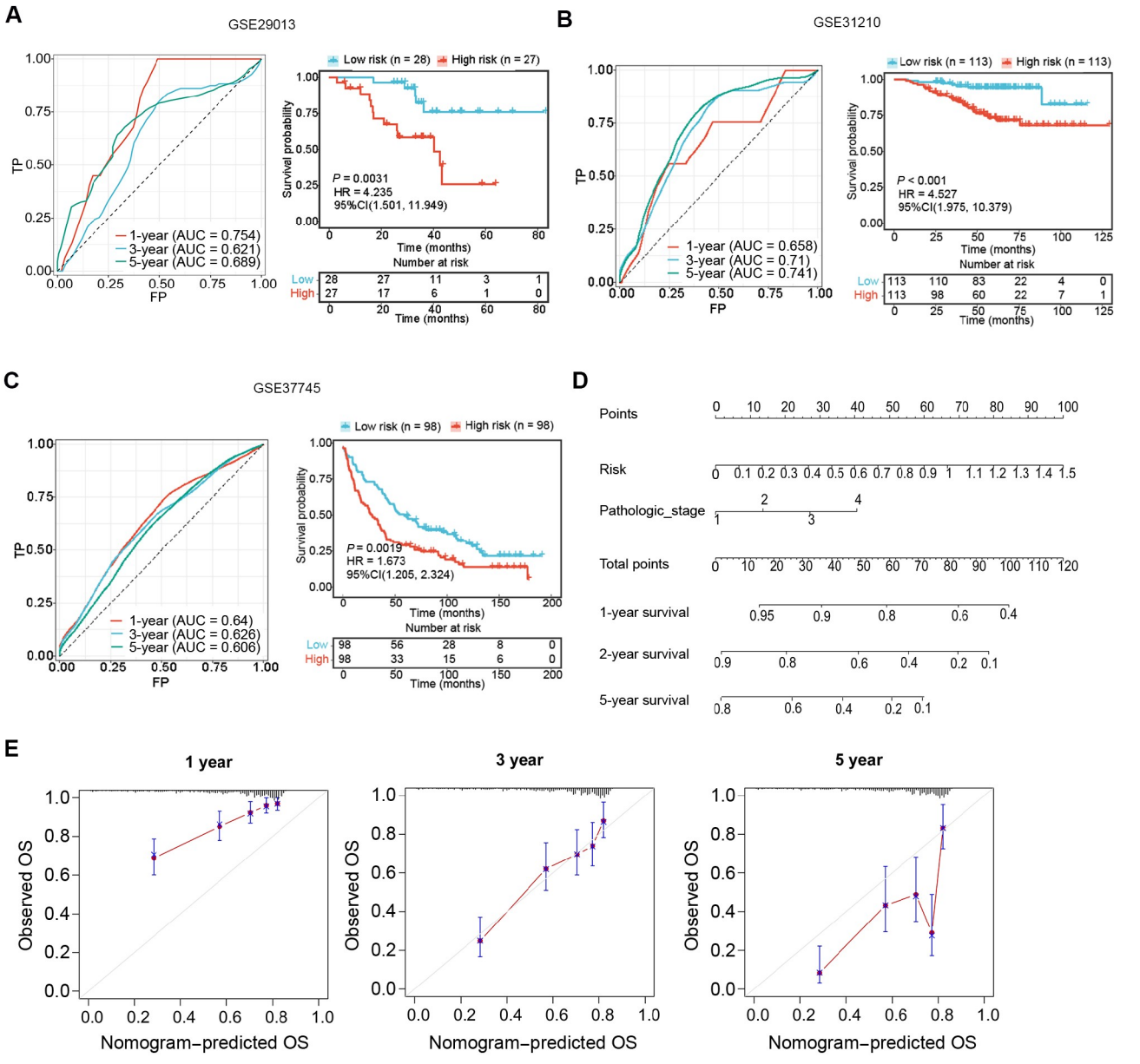

Fig. 4 Establishment and assessment of nomogram survival model. (A) Overall survival of patients in low- and high-risk groups in the GSE29013 cohorts. (B) Overall survival of patients in low- and high-risk groups in the GSE31210 cohorts. (C) Overall survival of patients in low- and high-risk groups in the GSE37745 cohorts. (D) A nomogram was established to predict the prognostic of NSCLC patients. (E) Calibration plots showing the probability of 1-, 3-, and 5-year overall survival in the TCGA cohorts.

These included *MUC2*, *NTSR1*, *FABP7*, *SPANXB1*, *IGFBP1*, *GCG*, *DKK4*, *PSG1*, *TAC3*, *MSTN*, and others (Fig. 6B). Gene ontology (GO) enrichment analysis showed the top 15 entries in the three categories of biological process (BP), cellular component (CC), and molecular function (MF). A circle diagram was used to display highly enriched entries and their corresponding genes, revealing that DEGs were involved in various biological pathways (Fig. 6C and 6D). Kyoto Encyclopedia of Genes and Genomes (KEGG) enrichment analysis revealed that these DEGs were involved in neuroactive ligand–receptor interaction, PI3K-Akt, AMPK, and other biological pathways (Fig. 6E). The genes corresponding with the top five enriched entries, namely, metabolic pathways, neuroactive ligand–receptor interaction, PI3K-Akt signaling pathway, pathways in cancer, and cytokine–cytokine receptor interaction, are shown in a circular diagram (Fig. 6F).

Tumor microenvironment and mtPCD signature

We used the CIBERSORT algorithm to analyze

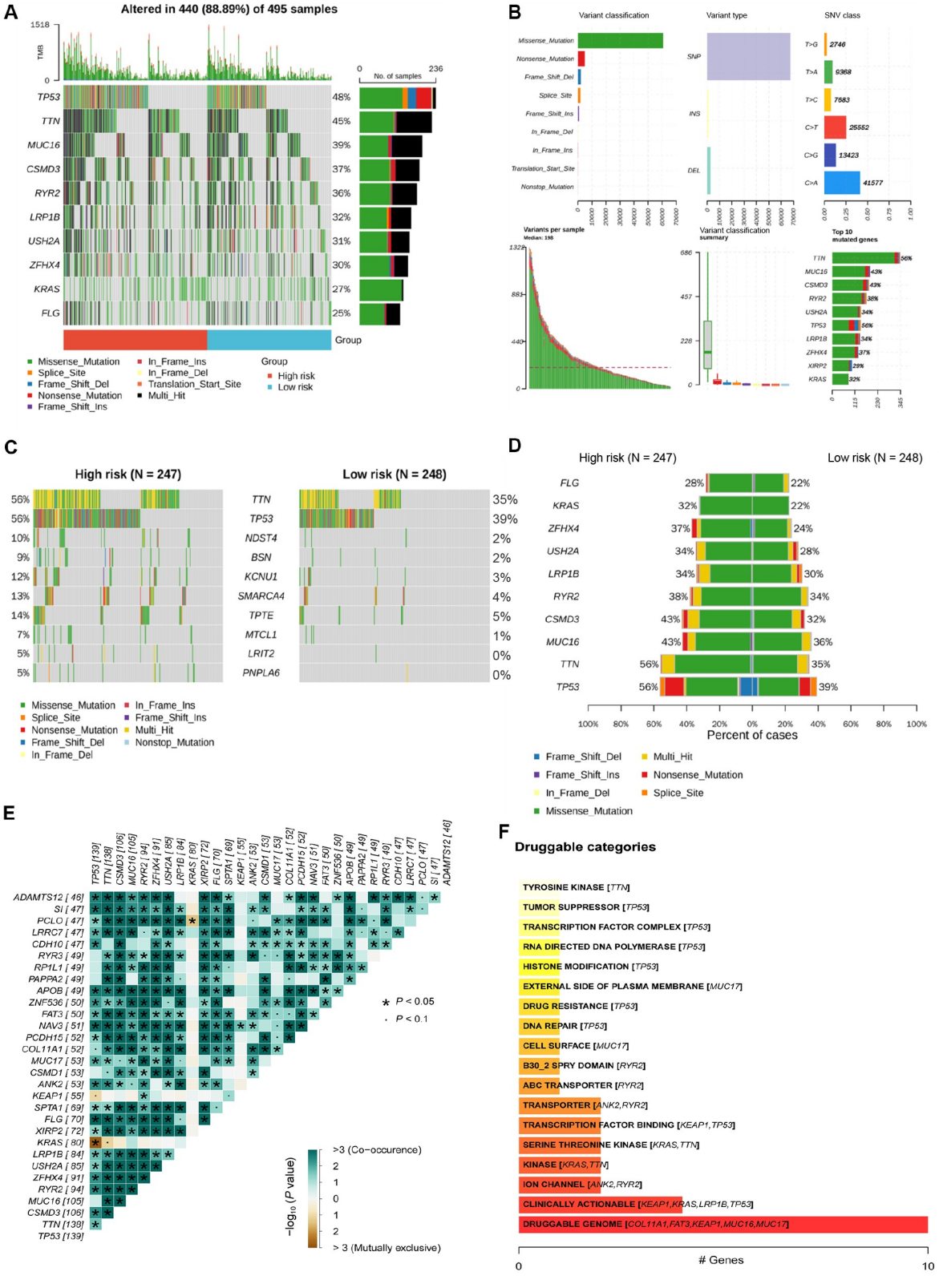

Fig. 5 Genomic variation landscape of mtPCD genes in NSCLC patients. (A) An oncoplot of prognostic mtPCD-related genes in the TCGA cohort. (B) An oncoplot of prognostic mtPCD-related genes in the high-risk group in the TCGA cohort. (C) Top 10 mutated gene frequency between high- and low-risk groups. (D) Difference in top 10 mutated gene frequency between high- and low-risk groups. (E) Correlation analysis between the top 30 mutated genes in the high-risk group. *P* values, Pearson correlation analysis. (F) Drug classification for predicting potentially druggable genes.

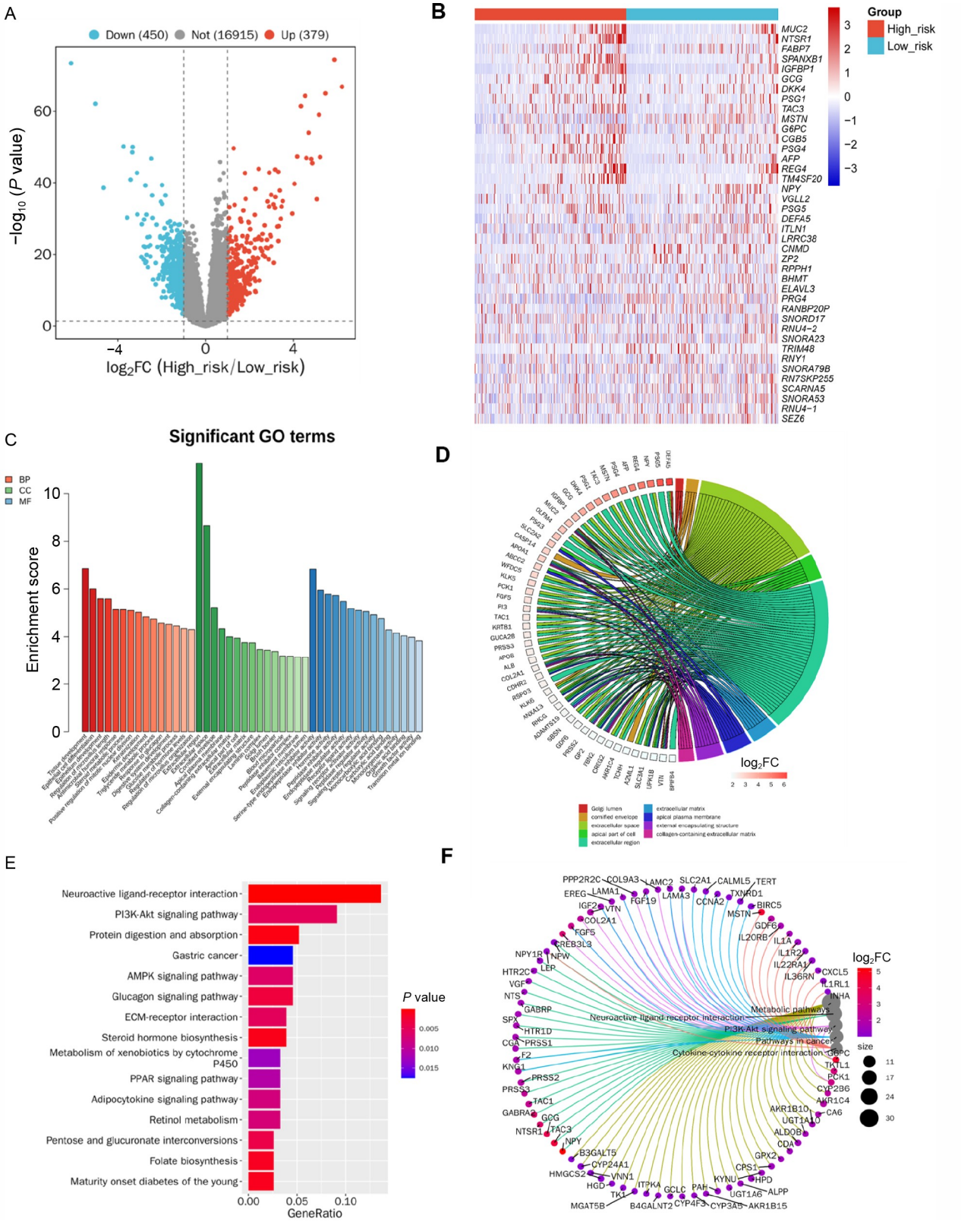

Fig. 6 Transcriptome variation landscape of mtPCD genes in NSCLC patients. (A) Volcano plot of mtPCD-related DEGs (green: downregulated DEGs; red: upregulated DEGs; gray: unchanged genes). $P < 0.05$ and $|\log_2 FC| > 2$. (B) Heatmap of the top 20 platelet-related DEGs between low-risk and high-risk groups. (C) GO enrichment analyses based on DEGs. (D) GO enrichment analysis circle diagram corresponding with some genes enriched by some items. (E) KEGG enrichment analyses based on the DEGs. (F) KEGG enrichment analysis circle diagram corresponding with some genes enriched by the top five entries.

differences in the tumor immune microenvironment (TME) between high- and low-risk groups. First, we analyzed the expression of various immune cells in the two groups and found that these cell populations were extensively present in all samples (Fig. 7A). We then analyzed the differences in the distribution characteristics of immune cells between the high- and low-risk groups and presented the result in the form of heat map and box plot, respectively (Fig. 7B and 7C). Results showed that the infiltration of Treg cells in the high-risk group was significantly higher than that in the low-risk group, which may cause immune escape (Fig. 7D). Subsequently, we analyzed the correlation among various types of immune cells and found more or less certain correlations between these immune cells (Fig. 7E). Furthermore, we found a significant difference in TME scores between the high- and low-risk groups (Fig. 7F–7I), and a high TME score was associated with a favorable response to immune-checkpoint inhibitor treatment. Thus, high-risk patients may be more suitable for immunotherapy. A significant difference in TMB scores between the high- and low-risk groups was also observed (Fig. 7J), with higher TMB scores corresponding with a positive immune-checkpoint inhibitor response. This finding further illustrated that patients with high-risk scores were the ones who can truly benefit from immunotherapy.

RIPK2 was overexpressed and inversely associated with overall survival of NSCLC

Next, we selected the gene from the above model that had not been functionally studied in NSCLC and had the highest prognostic hazard ratio for validation. RIPK2 acts as a key effector of NOD1 and NOD2 signaling pathways, involved in various physiologic processes such as immune response, growth control, and anti-apoptosis protection [44]. We analyzed the expression of *RIPK2* in tumor and counterpart normal tissues of various types of cancers using TCGA datasets and found that *RIPK2* expression was found to be significantly higher in the vast majority of tumor tissues than normal ones (Fig. 8A). We tested the potential association between the expression level of *RIPK2* and survival time of the patients, and found that *RIPK2* level was inversely associated with the OS of patients with uveal melanoma, thymoma, kidney papillary cell carcinoma, and LUAD (Fig. 8B).

Meanwhile, we examined the expression of RIPK2 in LUAD tissues and found that RIPK2 expression was significantly higher in tumor tissues than in normal ones (Fig. 8C). Then, we performed IHC assay on FFPE samples from 63 treatment-naïve patients to test RIPK2 expression (Table 3). The IRS was calculated, and the median expression level was used as a cutoff value. We found that tumor tissues were expressed at a much higher level of RIPK2, whereas normal lung tissues were expressed at a lower level (Fig. 8D and 8E). Moreover, 38 (60.3%) patients exhibited a high level, whereas 25 (39.7%) cases had a low level of RIPK2 (Fig. 8D and 8E). Using the Kaplan–Meier method, we analyzed the potential association between the expression level of RIPK2 and clinical outcome in 44 patients whose survival information was available. Patients with a high level of RIPK2 had significantly poorer OS than those with a low level of RIPK2 (Fig. 8F).

RIPK2 is required for NSCLC cell proliferation

To investigate the role of RIPK2 in NSCLC, we knocked down its expression in NSCLC cell lines H1299 and A549 (Fig. 9A) and observed that the proliferation of these cells was significantly inhibited (Fig. 9B). After *RIPK2* knockdown, the colony-formation ability of H1299 and A549 cells was observably reduced (Fig. 9C), and the proportion of apoptosis significantly increased (Fig. 9D). Moreover, si*RIPK2* treatment led to the downregulation of Bcl2, p-Akt, p-ERK, and p-P65 and the upregulation of Bax (Fig. 9E). To test this observation *in vivo*, si*RIPK2*-transfected A549 cells were injected into the right flank of NSG mice with severe combined immunodeficiency. We found that compared with the control, RIPK2 knockdown significantly inhibited tumor growth and reduced tumor volume and weight (Fig. 9F–9H). These results indicated that RIPK2 was an oncogene in NSCLC, consistent with our model predictions.

Discussion

This study is the first to provide a comprehensive analysis of 12 different mtPCD modes. A cell-death signature in TCGA NSCLC cohort was constructed, and its performance was validated in three other external cohorts (GSE29013, GSE31210, and GSE37745). A nomogram combining the clinical characteristics of NSCLC patients and mtPCD-related gene expression pattern was established and shown to perform well in predicting prognosis. Similarly, we determined that mtPCD genes were strongly associated with immune-cell infiltration and the response to immunotherapy.

mtPCD is a cell-death process mediated by molecular programs with the regulated specific genes and plays a key role in the normal development and maintenance of homeostasis in organism [45, 46]. A signature with 18 mtPCD-related genes (*AP3S1*, *CCK*, *EIF2AK3*, *ERO1A*, *KRT8*, *PEBP1*, *PIK3CD*, *PPIA*, *PPP3CC*, *RAB39B*, *RIPK2*, *RUBCNL*, *SELENOK*, *SQLE*, *STK3*, *TRIM6*, *VDAC1*, and *VPS13D*) was identified and confirmed to predict the OS of NSCLC patients with extremely high accuracy. Notably, AP3S1 is overexpressed in most tumors and significantly correlated inversely with

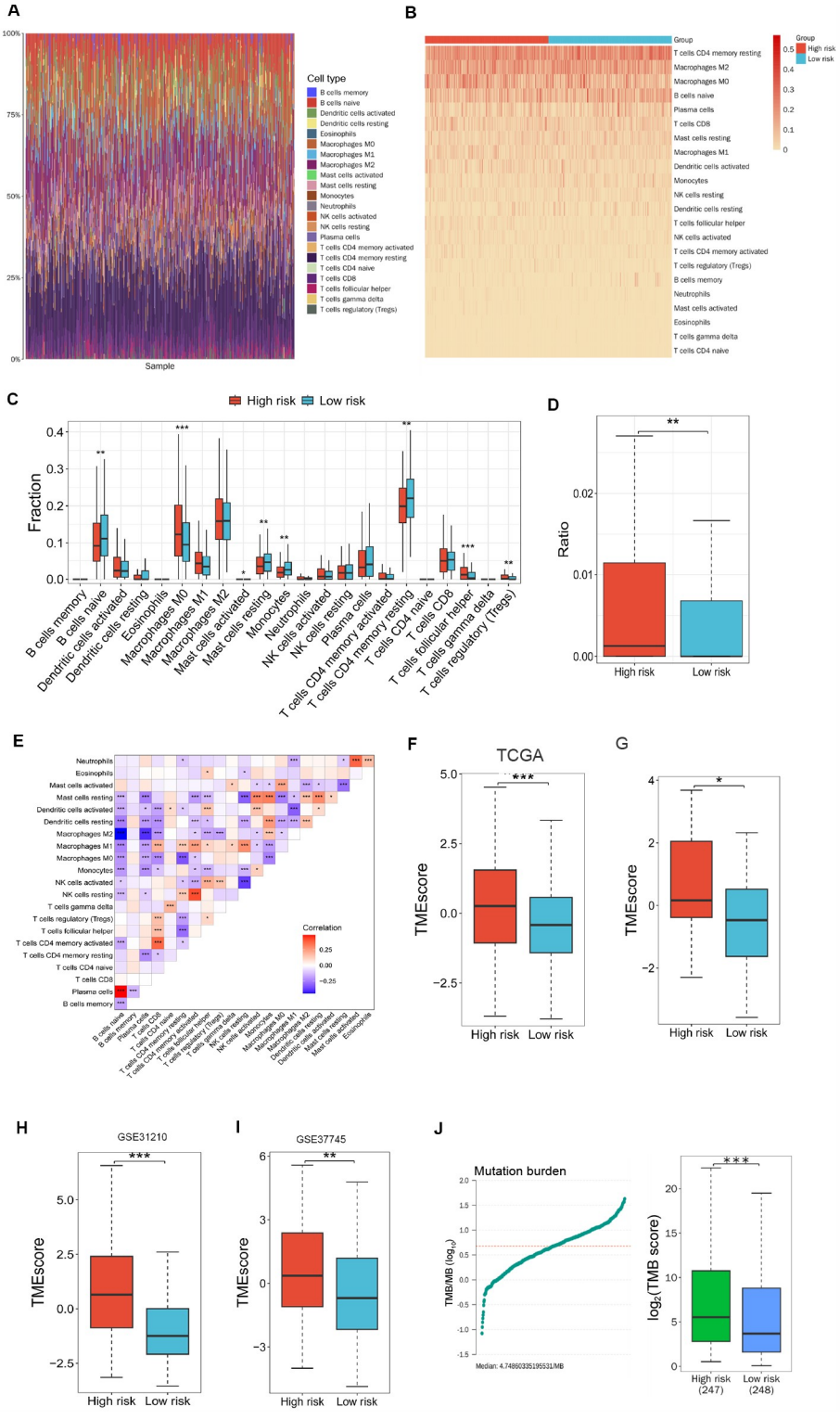

Fig. 7 Dissection of tumor microenvironment based on mtPCD signature. (A) Heat map of immune-cell expression in all samples. (B) Heat map of immune-cell expression separately in samples from the high- and low-risk groups. (C) Box plots of immune cells expressed separately in samples from the high- and low-risk groups. *P* values, Student's *t* test. **P* < 0.05, ***P* < 0.01, ****P* < 0.001. (D) Box plots of Treg cells expressed separately in samples from the high- and low-risk groups. *P* values, Student's *t* test. ***P* < 0.01. (E) Correlation analysis between the expression of various immune cells. *P* values, Pearson correlation analysis. **P* < 0.05, ***P* < 0.01, ****P* < 0.001. (F-I) Box plots of TME scores in the high- and low-risk groups of the TCGA, GSE29013, GSE31210, and GSE37745 cohorts, respectively. *P* values, Student's *t* test. **P* < 0.05, ***P* < 0.01, ****P* < 0.001. (J) Plot of the relationship between TMB and risk values. *P* values, Student's *t* test. ****P* < 0.001.

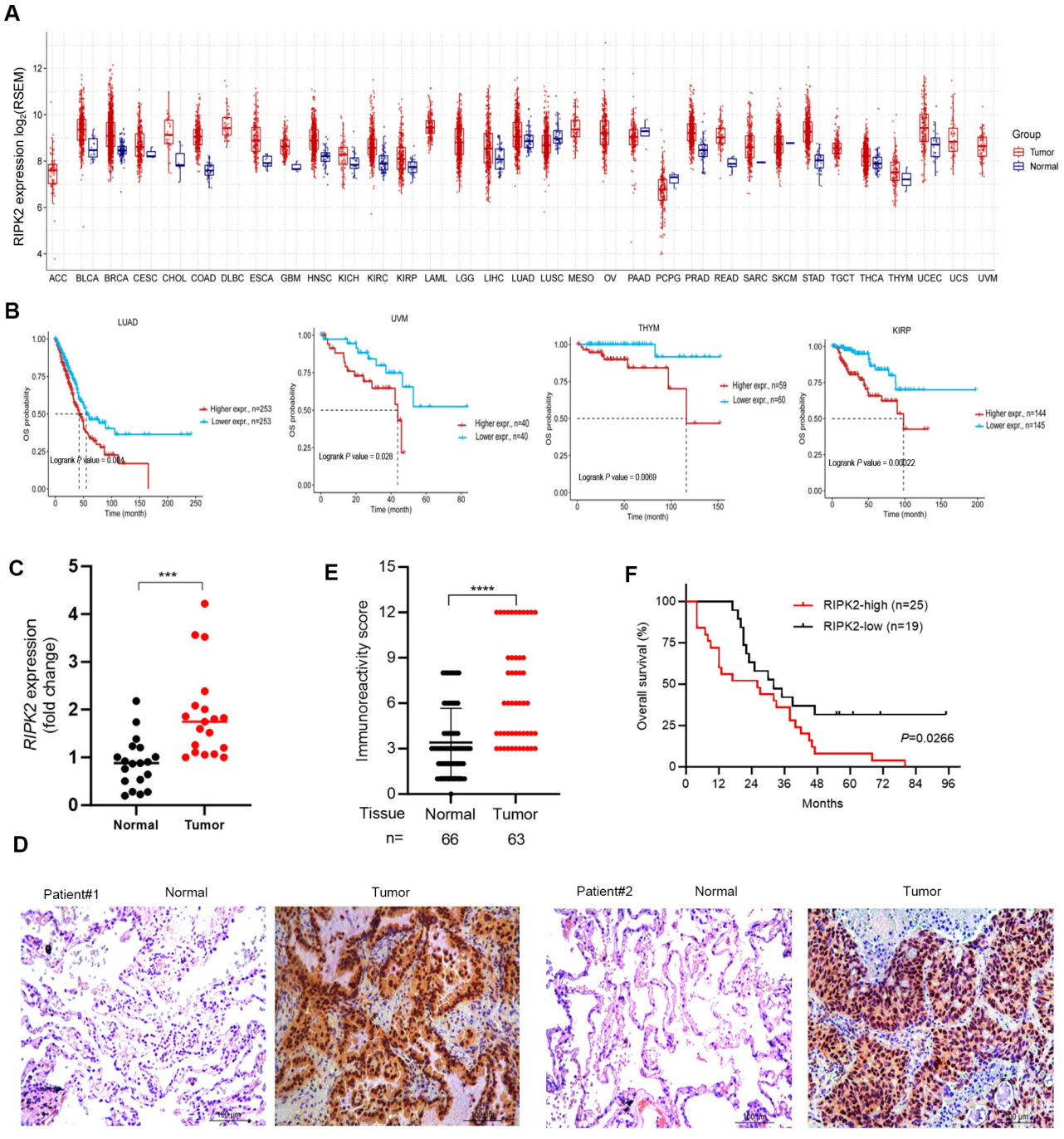

Fig. 8 RIPK2 is overexpressed in NSCLCs and inversely associated with survival time of the patients. (A) Expression level of *RIPK2* in indicated tumors and their counterpart normal tissues from TCGA datasets. (B) Overall survival of patients with indicated subtype of cancer and high or low *RIPK2* expression levels. *P* values were calculated by log-rank test. Data were from the TCGA database. LUAD, lung adenocarcinoma; UVM, uveal melanoma; THYM, thymoma. kidney papillary cell carcinoma, KIRP. (C) Expression level of *RIPK2* in tumors and counterpart normal tissues from LUAD patients. *P* values, Student's *t* test. ***$P < 0.001$. (D, E) RIPK2 in NSCLC patient samples was detected by immunohistochemistry assay (D), and the immunoreactivity score (IRS) was calculated (E). *P* values, Student's *t* test. ****$P < 0.0001$. (F) Overall survival of NSCLC patients. *P* value, log-rank test.

survival [47]. Herein, we found that AP3S1 was a risk factor for NSCLC survival. CCK is a neuropeptide that regulates digestion, neurotransmitters, and memory [48]. CCK expression and NSCLC survival were found to be inversely correlated. ERO1A can promote breast cancer metastasis [49], target ERO1A, and activate anti-tumor immunity [50]. Our study found that high ERO1A was associated with poor prognosis of NSCLCs. KRT8 is abnormally expressed in LUAD and is inversely associated with patient prognosis [51], as confirmed in

Table 3 Baseline characteristics of 63 patients with NSCLC

Characteristics	Total	RIPK2-low, *n* (%)	RIPK2-high, *n* (%)	*P* value
n	63	25 (39.7)	38 (60.3)	
Age				
⩽ 60	24	13 (54.2)	11 (45.8)	0.6
> 60	39	25 (64.1)	14 (35.9)	
Sex				
Male	37	22 (59.5)	15 (40.5)	0.99
Female	26	16 (61.5)	10 (38.5)	
Greatest tumor diameter				
< 4	34	23 (67.6)	11 (32.4)	
⩾ 4	22	10 (46.2)	12 (53.8)	0.24
Unknown	7	5 (71.4)	2 (28.6)	
Histologic grade				
⩽ II	34	21 (61.8)	13 (38.2)	0.99
> II	29	17 (58.6)	12 (41.4)	
Stage				
I–II	24	15 (62.5)	9 (37.5)	
III–IV	23	11 (47.8)	12 (52.2)	0.23
Unknown	16	12 (75)	4 (25)	

P value, Fisher's exact test.

our study. VPS13D deletion leads to impaired mitophagy, whereas VPS13D mutation leads to VPS13D-related dyskinesia [52]. VPS13D was a prognostic factor for NSCLC OS in our study. SQLE attenuates ER stress and promotes pancreatic cancer growth [53], consistent with our finding that high SQLE expression level was associated with poor prognosis in NSCLC. STK3 promotes pancreatic cancer cell proliferation through the PI3K/Akt pathway [54], and our results indicated that STK3 was negatively correlated with NSCLC OS. PPP3CC has been proven to promote the apoptosis of epithelial cells and inhibit tumor proliferation in ovarian cancer [55], and we also found that it was a prognostic factor for NSCLC OS through the prognostic model. VDAC1 is located on the outer mitochondrial membrane and regulates energy production. Studies have shown that VDAC1 is overexpressed in breast cancer and is associated with the suppression of tumor immunity [56]. Similarly, our data showed that VDAC1 was a risk factor in NSCLC. As a key regulator of the cell-death pathway, RIPK2 has become a target for cancer therapy [44]. Herein, we also identified RIPK2 as a risk factor for NSCLC. Given that RIPK2 had the highest hazard ratio among all genes in our model that had not been functionally studied in NSCLC, we performed relevant validation and found that RIPK2 was highly expressed in NSCLC. It was inversely associated as well with the survival time of the patients. Tumor-cell proliferation was inhibited when RIPK2 was silenced, indicating that RIPK2 acts as an oncogene in NSCLC, consistent with our model predictions.

Immunotherapy has substantially improved the OS of patients with unresectable tumors [57]. In general, decreased infiltration of antitumor immune cells and increased infiltration of pro-tumor immune cells indicate that the TME is compromised [58–60]. Treg cells exert immunosuppressive effects and inhibit the immune responses of other immune cells [61]. Our results showed that Treg cell infiltration was significantly higher in the high-risk group than in the low-risk one. The high-risk group patients may exhibit immune escape, resulting in poor patient prognosis. A significant difference in TME scores also existed between the high- and low-risk groups, and a high TME score corresponded with a positive response to immune-checkpoint inhibitor treatment [62]. Therefore, based on these results, we speculated that the high-risk patients in this study may be more suitable for immunotherapy. We further found a significant difference in the TMB scores between the high- and low-risk groups. Higher TMB scores corresponded with a more active response to immune-checkpoint inhibitors [63], suggesting that high-risk patients may benefit from immunotherapy.

Although mtPCD may serve as an independent prognostic factor for NSCLC and our model showed good performance in training and validation datasets, our study still had some limitations. First, the patients were recruited retrospectively, which may have inevitably led

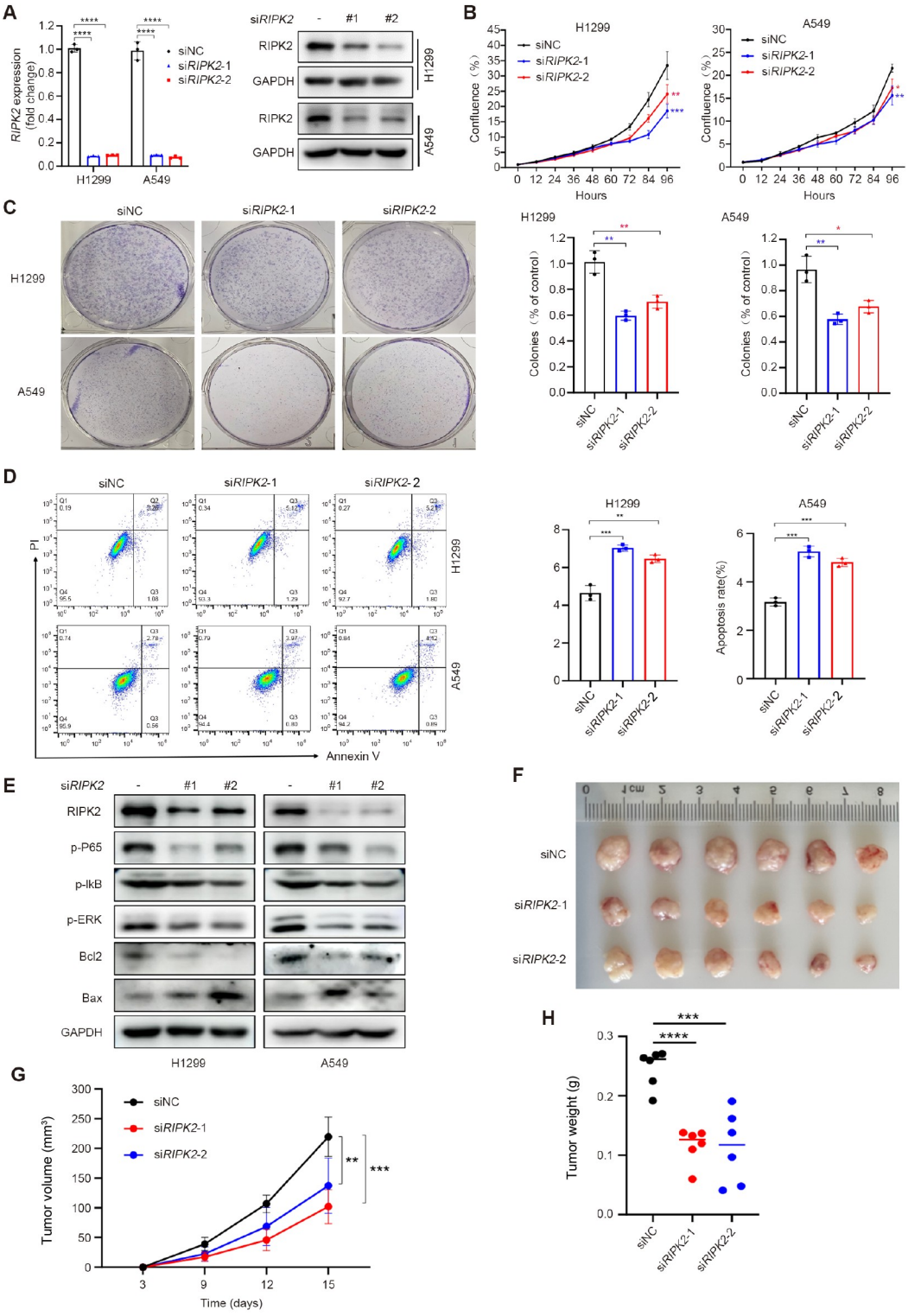

Fig. 9 RIPK2 is required for NSCLC cell proliferation. (A) Expression of RIPK2 in H1299 and A549 cells transfected with si*RIPK2* as detected by real-time RT-PCR and Western blot. *P* values, Student's *t* test. ****$P < 0.0001$. (B) Cell proliferation of H1299 and A549 cells transfected with si*RIPK2* measured using an IncuCyte Live-Cell Analysis System. *P* values, Student's *t* test. *$P < 0.05$, **$P < 0.01$, ***$P < 0.001$. (C) Colony-formation activity of H1299 and A549 cells transfected with si*RIPK2*. *P* values, Student's *t* test. *$P < 0.05$, **$P < 0.01$. (D) Apoptosis assay of H1299 and A549 cells transfected with si*RIPK2*. *P* values, Student's *t* test. **$P < 0.01$, ***$P < 0.001$. (E) H1299 and A549 cells were transfected with si*RIPK2*, and cell lysates were subjected to Western blot using the indicated antibodies. (F–H) Knockdown of *RIPK2* inhibited tumor growth, and the tumor volume and tumor weight were measured. *Ex vivo* images of resected tumors (F) and growth curves of tumor volume (G) and weight (H) are shown. *P* values, Student's *t* test. **$P < 0.01$, ***$P < 0.001$, ****$P < 0.0001$.

to bias. Second, their clinical information was obtained from public databases and lacked validation using our own independent external cohort. Therefore, more in-depth studies such as prospective clinical studies with high quality, large sample sizes, and sufficient follow-up data for additional validation are needed to investigate the feasibility of using this model to predict prognosis and guide NSCLC treatment.

A variety of agents targeting PCD are being developed for potential clinical applications. For example, the small-molecule compound resibufogenin inhibits colorectal cancer development and metastasis by inducing receptor-interacting protein kinase 3-mediated necrosis [64]. Simvastatin induces pyroptosis and inhibits NSCLC cell migration by the activation of NACHT, LRR, and PYD domains-containing protein 3 inflammasome and caspase-1 [65]. Artesunate, a derivative of artemisinin, inhibits ovarian cancer cell proliferation by increasing reactive oxygen species production and triggering ferroptosis [66]. The administration of nanoparticles can reverse cisplatin resistance in cancer cells by inducing cuproptosis [67]. Additionally, the induction of ferroptosis can improve the therapeutic efficacy of immune-checkpoint inhibitors [68]. More studies should be performed to determine the therapeutic potentials of PCD-targeting agents in NSCLC.

Acknowledgements

This work was supported by the National Key Research and Development Program of China (Nos. 2023YFC3503205 and 2022YFA1103900), the CAMS Innovation Fund for Medical Sciences (CIFMS; No. 2022-I2M-1-009), the National Natural Science Foundation of China (Nos. 82372944, 82073092 and 82273076), the Science and Technology Research Project of Henan Province (No. 222102310636), the Henan Provincial Medical Science and Technology Research Project (No. LHGJ20210183), and the Scientific Research Fund Project of the Affiliated Cancer Hospital of Zhengzhou University & Henan Cancer Hospital.

Compliance with ethics guidelines

Conflicts of interest Xueyan Shi, Sichong Han, and Guizhen Wang declare that they have no conflict of interest. Guangbiao Zhou is the Executive Deputy Editor-in-Chief of *Frontiers of Medicine*, who was excluded from the peer-review process and all editorial decisions related to the acceptance and publication of this article. Peer-review was handled independently by the other editors to minimise bias.

The study was approved by the Ethics Committee of Cancer Hospital, Chinese Academy of Medical Sciences and the study was performed in accordance with the ethical standards as laid down in the 1964 *Declaration of Helsinki* and its later amendments or comparable ethical standards. Informed consent was obtained from all patients for being included in the study. All institutional and national guidelines for the care and use of laboratory animals were followed.

References

1. The International Agency for Research on Cancer (IARC) of the World Health Organization. Global cancer burden growing, amidst mounting need for services. 2024. Available at the website of WHO
2. Nicholson AG, Tsao MS, Beasley MB, Borczuk AC, Brambilla E, Cooper WA, Dacic S, Jain D, Kerr KM, Lantuejoul S, Noguchi M, Papotti M, Rekhtman N, Scagliotti G, van Schil P, Sholl L, Yatabe Y, Yoshida A, Travis WD. The 2021 WHO classification of lung tumors: impact of advances Since 2015. J Thorac Oncol 2022; 17(3): 362–387
3. Tsuboi M, Herbst RS, John T, Kato T, Majem M, Grohé C, Wang J, Goldman JW, Lu S, Su WC, de Marinis F, Shepherd FA, Lee KH, Le NT, Dechaphunkul A, Kowalski D, Poole L, Bolanos A, Rukazenkov Y, Wu YL. Overall survival with osimertinib in resected EGFR-mutated NSCLC. N Engl J Med 2023; 389(2): 137–147
4. Garon EB, Rizvi NA, Hui R, Leighl N, Balmanoukian AS, Eder JP, Patnaik A, Aggarwal C, Gubens M, Horn L, Carcereny E, Ahn MJ, Felip E, Lee JS, Hellmann MD, Hamid O, Goldman JW, Soria JC, Dolled-Filhart M, Rutledge RZ, Zhang J, Lunceford JK, Rangwala R, Lubiniecki GM, Roach C, Emancipator K, Gandhi L. Pembrolizumab for the treatment of non-small-cell lung cancer. N Engl J Med 2015; 372(21): 2018–2028
5. Xiao C, Xiong W, Xu Y, Zou J, Zeng Y, Liu J, Peng Y, Hu C, Wu F. Immunometabolism: a new dimension in immunotherapy resistance. Front Med 2023; 17(4): 585–616
6. Zhong J, Bai H, Wang Z, Duan J, Zhuang W, Wang D, Wan R, Xu J, Fei K, Ma Z, Zhang X, Wang J. Treatment of advanced non-small cell lung cancer with driver mutations: current applications and future directions. Front Med 2023; 17(1): 18–42
7. Liao L, Xu H, Zhao Y, Zheng X. Metabolic interventions combined with CTLA-4 and PD-1/PD-L1 blockade for the treatment of tumors: mechanisms and strategies. Front Med 2023; 17(5): 805–822
8. Hu X, Khatri U, Shen T, Wu J. Progress and challenges in RET-targeted cancer therapy. Front Med 2023; 17(2): 207–219
9. Garassino MC, Gadgeel S, Speranza G, Felip E, Esteban E, Dómine M, Hochmair MJ, Powell SF, Bischoff HG, Peled N, Grossi F, Jennens RR, Reck M, Hui R, Garon EB, Kurata T, Gray JE, Schwarzenberger P, Jensen E, Pietanza MC, Rodríguez-Abreu D. Pembrolizumab plus pemetrexed and platinum in nonsquamous non-small-cell lung cancer: 5-year outcomes from the phase 3 KEYNOTE-189 study. J Clin Oncol 2023; 41(11): 1992–1998
10. Novello S, Kowalski DM, Luft A, Gümüş M, Vicente D, Mazières J, Rodríguez-Cid J, Tafreshi A, Cheng Y, Lee KH, Golf A, Sugawara S, Robinson AG, Halmos B, Jensen E, Schwarzenberger P, Pietanza MC, Paz-Ares L. Pembrolizumab plus chemotherapy in squamous non-small-cell lung cancer: 5-year update of the phase III KEYNOTE-407 study. J Clin Oncol 2023; 41(11): 1999–2006
11. Blaquier JB, Ortiz-Cuaran S, Ricciuti B, Mezquita L, Cardona AF, Recondo G. Tackling osimertinib resistance in EGFR-mutant non-small cell lung cancer. Clin Cancer Res 2023; 29(18): 3579–3591
12. Passaro A, Jänne PA, Mok T, Peters S. Overcoming therapy

resistance in EGFR-mutant lung cancer. Nat Cancer 2021; 2(4): 377–391
13. Zhang H, Wang Y, Yuan X, Zou Y, Xiong H. Research progress on lung cancer stem cells in epidermal growth factor receptor–tyrosine kinase inhibitor targeted therapy resistance in lung adenocarcinoma. Oncol Transl Med 2024; 10(1): 42–46
14. Memon D, Schoenfeld AJ, Ye D, Fromm G, Rizvi H, Zhang X, Keddar MR, Mathew D, Yoo KJ, Qiu J, Lihm J, Miriyala J, Sauter JL, Luo J, Chow A, Bhanot UK, McCarthy C, Vanderbilt CM, Liu C, Abu-Akeel M, Plodkowski AJ, McGranahan N, Łuksza M, Greenbaum BD, Merghoub T, Achour I, Barrett JC, Stewart R, Beltrao P, Schreiber TH, Minn AJ, Miller ML, Hellmann MD. Clinical and molecular features of acquired resistance to immunotherapy in non-small cell lung cancer. Cancer Cell 2024; 42(2): 209–224.e9
15. Newton K, Strasser A, Kayagaki N, Dixit VM. Cell death. Cell 2024; 187(2): 235–256
16. Peng F, Liao M, Qin R, Zhu S, Peng C, Fu L, Chen Y, Han B. Regulated cell death (RCD) in cancer: key pathways and targeted therapies. Signal Transduct Target Ther 2022; 7(1): 286
17. Park W, Wei S, Kim BS, Kim B, Bae SJ, Chae YC, Ryu D, Ha KT. Diversity and complexity of cell death: a historical review. Exp Mol Med 2023; 55(8): 1573–1594
18. Zou Y, Xie J, Zheng S, Liu W, Tang Y, Tian W, Deng X, Wu L, Zhang Y, Wong CW, Tan D, Liu Q, Xie X. Leveraging diverse cell-death patterns to predict the prognosis and drug sensitivity of triple-negative breast cancer patients after surgery. Int J Surg 2022; 107: 106936
19. Medina CB, Mehrotra P, Arandjelovic S, Perry JSA, Guo Y, Morioka S, Barron B, Walk SF, Ghesquière B, Krupnick AS, Lorenz U, Ravichandran KS. Metabolites released from apoptotic cells act as tissue messengers. Nature 2020; 580(7801): 130–135
20. Negroni A, Colantoni E, Cucchiara S, Stronati L. Necroptosis in intestinal inflammation and cancer: new concepts and therapeutic perspectives. Biomolecules 2020; 10: 1431
21. Sun L, Wang H, Wang Z, He S, Chen S, Liao D, Wang L, Yan J, Liu W, Lei X, Wang X. Mixed lineage kinase domain-like protein mediates necrosis signaling downstream of RIP3 kinase. Cell 2012; 148(1–2): 213–227
22. Shi J, Zhao Y, Wang Y, Gao W, Ding J, Li P, Hu L, Shao F. Inflammatory caspases are innate immune receptors for intracellular LPS. Nature 2014; 514(7521): 187–192
23. Orning P, Weng D, Starheim K, Ratner D, Best Z, Lee B, Brooks A, Xia S, Wu H, Kelliher MA, Berger SB, Gough PJ, Bertin J, Proulx MM, Goguen JD, Kayagaki N, Fitzgerald KA, Lien E. Pathogen blockade of TAK1 triggers caspase-8-dependent cleavage of gasdermin D and cell death. Science 2018; 362(6418): 1064–1069
24. Dixon SJ, Lemberg KM, Lamprecht MR, Skouta R, Zaitsev EM, Gleason CE, Patel DN, Bauer AJ, Cantley AM, Yang WS, Morrison B III, Stockwell BR. Ferroptosis: an iron-dependent form of nonapoptotic cell death. Cell 2012; 149(5): 1060–1072
25. Stockwell BR, Friedmann Angeli JP, Bayir H, Bush AI, Conrad M, Dixon SJ, Fulda S, Gascón S, Hatzios SK, Kagan VE, Noel K, Jiang X, Linkermann A, Murphy ME, Overholtzer M, Oyagi A, Pagnussat GC, Park J, Ran Q, Rosenfeld CS, Salnikow K, Tang D, Torti FM, Torti SV, Toyokuni S, Woerpel KA, Zhang DD. Ferroptosis: a regulated cell death nexus linking metabolism, redox biology, and disease. Cell 2017; 171(2): 273–285
26. Tsvetkov P, Coy S, Petrova B, Dreishpoon M, Verma A, Abdusamad M, Rossen J, Joesch-Cohen L, Humeidi R, Spangler RD, Eaton JK, Frenkel E, Kocak M, Corsello SM, Lutsenko S, Kanarek N, Santagata S, Golub TR. Copper induces cell death by targeting lipoylated TCA cycle proteins. Science 2022; 375(6586): 1254–1261
27. Mizushima N, Komatsu M. Autophagy: renovation of cells and tissues. Cell 2011; 147(4): 728–741
28. Neuenfeldt F, Schumacher JC, Grieshaber-Bouyer R, Habicht J, Schröder-Braunstein J, Gauss A, Merle U, Niesler B, Heineken N, Dalpke A, Gaida MM, Giese T, Meuer S, Samstag Y, Wabnitz G. Inflammation induces pro-NETotic neutrophils via TNFR2 signaling. Cell Rep 2022; 39(3): 110710
29. Zhou Y, Liu L, Tao S, Yao Y, Wang Y, Wei Q, Shao A, Deng Y. Parthanatos and its associated components: promising therapeutic targets for cancer. Pharmacol Res 2021; 163: 105299
30. Nakamura H, Tanaka T, Zheng C, Afione SA, Warner BM, Noguchi M, Atsumi T, Chiorini JA. Lysosome-associated membrane protein 3 induces lysosome-dependent cell death by impairing autophagic caspase 8 degradation in the salivary glands of individuals with Sjögren's disease. Arthritis Rheumatol 2023; 75(9): 1586–1598
31. Chen F, Kang R, Liu J, Tang D. Mechanisms of alkaliptosis. Front Cell Dev Biol 2023; 11: 1213995
32. Lee AR, Park CY. Orai1 is an entotic Ca^{2+} channel for non-apoptotic cell death, entosis in cancer development. Adv Sci (Weinh) 2023; 10(14): 2205913
33. Holze C, Michaudel C, Mackowiak C, Haas DA, Benda C, Hubel P, Pennemann FL, Schnepf D, Wettmarshausen J, Braun M, Leung DW, Amarasinghe GK, Perocchi F, Staeheli P, Ryffel B, Pichlmair A. Oxeiptosis, a ROS-induced caspase-independent apoptosis-like cell-death pathway. Nat Immunol 2018; 19(2): 130–140
34. Bock FJ, Tait SWG. Mitochondria as multifaceted regulators of cell death. Nat Rev Mol Cell Biol 2020; 21(2): 85–100
35. Vringer E, Tait SWG. Mitochondria and cell death-associated inflammation. Cell Death Differ 2023; 30(2): 304–312
36. Nguyen TT, Wei S, Nguyen TH, Jo Y, Zhang Y, Park W, Gariani K, Oh CM, Kim HH, Ha KT, Park KS, Park R, Lee IK, Shong M, Houtkooper RH, Ryu D. Mitochondria-associated programmed cell death as a therapeutic target for age-related disease. Exp Mol Med 2023; 55(8): 1595–1619
37. Friedman J, Hastie T, Tibshirani R. Regularization paths for generalized linear models via coordinate descent. J Stat Softw 2010; 33(1): 1–22
38. Mayakonda A, Lin DC, Assenov Y, Plass C, Koeffler HP. Maftools: efficient and comprehensive analysis of somatic variants in cancer. Genome Res 2018; 28(11): 1747–1756
39. Wu T, Hu E, Xu S, Chen M, Guo P, Dai Z, Feng T, Zhou L, Tang W, Zhan L, Fu X, Liu S, Bo X, Yu G. clusterProfiler 4.0: a universal enrichment tool for interpreting omics data. Innovation (Camb) 2021; 2(3): 100141
40. Chen B, Khodadoust MS, Liu CL, Newman AM, Alizadeh AA. Profiling tumor infiltrating immune cells with CIBERSORT. Methods Mol Biol 2018; 1711: 243–259
41. Zeng D, Wu J, Luo H, Li Y, Xiao J, Peng J, Ye Z, Zhou R, Yu Y, Wang G, Huang N, Wu J, Rong X, Sun L, Sun H, Qiu W, Xue Y, Bin J, Liao Y, Li N, Shi M, Kim KM, Liao W. Tumor microenvironment evaluation promotes precise checkpoint immunotherapy of advanced gastric cancer. J Immunother Cancer

2021; 9(8): e002467
42. Xie D, Wang Z, Sun B, Qu L, Zeng M, Feng L, Guo M, Wang G, Hao J, Zhou G. High frequency of alternative splicing variants of the oncogene focal adhesion kinase in neuroendocrine tumors of the pancreas and breast. Front Med 2023; 17(5): 907–923
43. Sun BB, Wang GZ, Han SC, Yang FY, Guo H, Liu J, Liu YT, Zhou GB. Oncogenic functions and therapeutic potentials of targeted inhibition of SMARCAL1 in small cell lung cancer. Cancer Lett 2024; 592: 216929
44. You J, Wang Y, Chen H, Jin F. RIPK2: a promising target for cancer treatment. Front Pharmacol 2023; 14: 1192970
45. Chen Y, Lewis W, Diwan A, Cheng EHY, Matkovich SJ, Dorn GW II. Dual autonomous mitochondrial cell death pathways are activated by Nix/BNip3L and induce cardiomyopathy. Proc Natl Acad Sci USA 2010; 107(20): 9035–9042
46. Winter JM, Yadav T, Rutter J. Stressed to death: Mitochondrial stress responses connect respiration and apoptosis in cancer. Mol Cell 2022; 82(18): 3321–3332
47. Wu G, Chen M, Ren H, Sha X, He M, Ren K, Qi J, Lin F. AP3S1 is a novel prognostic biomarker and correlated with an immunosuppressive tumor microenvironment in pan-cancer. Front Cell Dev Biol 2022; 10: 930933
48. Reich N, Hölscher C. Cholecystokinin (CCK): a neuromodulator with therapeutic potential in Alzheimer's and Parkinson's disease. Front Neuroendocrinol 2024; 73: 101122
49. Zilli F, Marques Ramos P, Auf der Maur P, Jehanno C, Sethi A, Coissieux MM, Eichlisberger T, Sauteur L, Rouchon A, Bonapace L, Pinto Couto J, Rad R, Jensen MR, Banfi A, Stadler MB, Bentires-Alj M. The NFIB-ERO1A axis promotes breast cancer metastatic colonization of disseminated tumour cells. EMBO Mol Med 2021; 13(4): e13162
50. Liu L, Li S, Qu Y, Bai H, Pan X, Wang J, Wang Z, Duan J, Zhong J, Wan R, Fei K, Xu J, Yuan L, Wang C, Xue P, Zhang X, Ma Z, Wang J. Ablation of ERO1A induces lethal endoplasmic reticulum stress responses and immunogenic cell death to activate anti-tumor immunity. Cell Rep Med 2023; 4(10): 101206
51. Shi X, Li T, Liu Y, Yin L, Xiao L, Fu L, Zhu Y, Chen H, Wang K, Xiao X, Zhang H, Tan S, Tan S. HSF1 protects sepsis-induced acute lung injury by inhibiting NLRP3 inflammasome activation. Front Immunol 2022; 13: 781003
52. Koh K, Ishiura H, Shimazaki H, Tsutsumiuchi M, Ichinose Y, Nan H, Hamada S, Ohtsuka T, Tsuji S, Takiyama Y. VPS13D-related disorders presenting as a pure and complicated form of hereditary spastic paraplegia. Mol Genet Genomic Med 2020; 8(3): e1108
53. Xu R, Song J, Ruze R, Chen Y, Yin X, Wang C, Zhao Y. SQLE promotes pancreatic cancer growth by attenuating ER stress and activating lipid rafts-regulated Src/PI3K/Akt signaling pathway. Cell Death Dis 2023; 14(8): 497
54. Chen J, Liu F, Wu J, Yang Y, He J, Wu F, Yang K, Li J, Jiang Z, Jiang Z. Effect of STK3 on proliferation and apoptosis of pancreatic cancer cells via PI3K/AKT/mTOR pathway. Cell Signal 2023; 106: 110642
55. Anastasiadou E, Messina E, Sanavia T, Labruna V, Ceccarelli S, Megiorni F, Gerini G, Pontecorvi P, Camero S, Perniola G, Venneri MA, Trivedi P, Lenzi A, Marchese C. Calcineurin gamma catalytic subunit PPP3CC inhibition by miR-200c-3p affects apoptosis in epithelial ovarian cancer. Genes (Basel) 2021; 12(9): 1400
56. Fang Y, Liu J, Zhang Q, She C, Zheng R, Zhang R, Chen Z, Chen C, Wu J. Overexpressed VDAC1 in breast cancer as a novel prognostic biomarker and correlates with immune infiltrates. World J Surg Oncol 2022; 20(1): 211
57. Lahiri A, Maji A, Potdar PD, Singh N, Parikh P, Bisht B, Mukherjee A, Paul MK. Lung cancer immunotherapy: progress, pitfalls, and promises. Mol Cancer 2023; 22(1): 40
58. Sun L, Su Y, Jiao A, Wang X, Zhang B. T cells in health and disease. Signal Transduct Target Ther 2023; 8(1): 235
59. Myers JA, Miller JS. Exploring the NK cell platform for cancer immunotherapy. Nat Rev Clin Oncol 2021; 18(2): 85–100
60. Wang C, Zheng X, Zhang J, Jiang X, Wang J, Li Y, Li X, Shen G, Peng J, Zheng P, Gu Y, Chen J, Lin M, Deng C, Gao H, Lu Z, Zhao Y, Luo M. CD300ld on neutrophils is required for tumour-driven immune suppression. Nature 2023; 621(7980): 830–839
61. Tay C, Tanaka A, Sakaguchi S. Tumor-infiltrating regulatory T cells as targets of cancer immunotherapy. Cancer Cell 2023; 41(3): 450–465
62. Patel RB, Hernandez R, Carlson P, Grudzinski J, Bates AM, Jagodinsky JC, Erbe A, Marsh IR, Arthur I, Aluicio-Sarduy E, Sriramaneni RN, Jin WJ, Massey C, Rakhmilevich AL, Vail D, Engle JW, Le T, Kim KM, Bednarz B, Sondel PM, Weichert J, Morris ZS. Low-dose targeted radionuclide therapy renders immunologically cold tumors responsive to immune checkpoint blockade. Sci Transl Med 2021; 13(602): eabb3631
63. Samstein RM, Lee CH, Shoushtari AN, Hellmann MD, Shen R, Janjigian YY, Barron DA, Zehir A, Jordan EJ, Omuro A, Kaley TJ, Kendall SM, Motzer RJ, Hakimi AA, Voss MH, Russo P, Rosenberg J, Iyer G, Bochner BH, Bajorin DF, Al-Ahmadie HA, Chaft JE, Rudin CM, Riely GJ, Baxi S, Ho AL, Wong RJ, Pfister DG, Wolchok JD, Barker CA, Gutin PH, Brennan CW, Tabar V, Mellinghoff IK, DeAngelis LM, Ariyan CE, Lee N, Tap WD, Gounder MM, D'Angelo SP, Saltz L, Stadler ZK, Scher HI, Baselga J, Razavi P, Klebanoff CA, Yaeger R, Segal NH, Ku GY, DeMatteo RP, Ladanyi M, Rizvi NA, Berger MF, Riaz N, Solit DB, Chan TA, Morris LGT. Tumor mutational load predicts survival after immunotherapy across multiple cancer types. Nat Genet 2019; 51(2): 202–206
64. Han Q, Ma Y, Wang H, Dai Y, Chen C, Liu Y, Jing L, Sun X. Resibufogenin suppresses colorectal cancer growth and metastasis through RIP3-mediated necroptosis. J Transl Med 2018; 16(1): 201
65. Wang F, Liu W, Ning J, Wang J, Lang Y, Jin X, Zhu K, Wang X, Li X, Yang F, Ma J, Xu S. Simvastatin suppresses proliferation and migration in non-small cell lung cancer via pyroptosis. Int J Biol Sci 2018; 14(4): 406–417
66. Greenshields AL, Shepherd TG, Hoskin DW. Contribution of reactive oxygen species to ovarian cancer cell growth arrest and killing by the anti-malarial drug artesunate. Mol Carcinog 2017; 56(1): 75–93
67. Lu Y, Pan Q, Gao W, Pu Y, He B. Reversal of cisplatin chemotherapy resistance by glutathione-resistant copper-based nanomedicine via cuproptosis. J Mater Chem B Mater Biol Med 2022; 10(33): 6296–6306
68. Deng J, Zhou M, Liao T, Kuang W, Xia H, Yin Z, Tan Q, Li Y, Song S, Zhou E, Jin Y. Targeting cancer cell ferroptosis to reverse immune checkpoint inhibitor therapy resistance. Front Cell Dev Biol 2022; 10: 818453